Int j simul model 22 (2023) 2, 233-244
Original scientific paper

CAVITATION EROSION MODELLING – COMPARISON OF DIFFERENT DRIVING PRESSURE APPROACHES

Kevorkijan, L.[*]; Pezdevsek, M.[**]; Bilus, I.[*] & Hren, G.[**]
[*] University of Maribor, Faculty of Mechanical Engineering, Smetanova 17, 2000 Maribor, Slovenia
[**] University of Maribor, Faculty of Energy Technology, Hočevarjev trg 1, 8270 Krško, Slovenia
E-Mail: ignacijo.bilus@um.si

Abstract
In this paper we compared different driving pressure approaches to calculate the cavitation potential energy from a source, which is transferred to a surface. The first approach used the reference pressure, the second approach used the pressure calculated at each timestep with no averaging, the third approach used the averaged pressure values from all timesteps included in one shedding cycle, and the last approach used pressure values from the steady state simulations results. The results show that for all formulations the averaged pressure values and steady state pressure values give similar results in terms of mean potential power distribution on the hydrofoil surface as in absolute values. The reference pressure approach gave similar results for the derivative and divergence formulation while for the source term the mean potential power distribution on the hydrofoil surface differs and the maximums were near the leading edge. The approach where we used no pressure averaging gave adequate results in terms of mean potential power distribution but differs from other approaches in absolute values which were considerably lower for all potential power formulations.
(Received in January 2023, accepted in March 2023. This paper was with the authors 2 weeks for 2 revisions.)

Key Words: Cavitation, Erosion Potential, Driving Pressure, Numerical Simulation

1. INTRODUCTION

In liquids, formation of vapour cavities can occur due to a local drop in pressure below the vapour pressure of the liquid. When the vapour cavity is subjected to a higher pressure in the surrounding liquid, the cavity collapses. This phenomenon is termed cavitation.

Following the vapour cavity collapse the pressure in the liquid suddenly increases causing vibrations, noise and potentially erosive damage to a nearby surface. Since cavitation occurs in many important, complex and expensive hydraulic systems, such as pumps [1], fuel injectors [2], marine propellers [3, 4] and hydraulic turbines [5], there is a need for further research of erosion due to cavitation.

Following the early theoretical research to understand the fundamentals of cavitation [6, 7] mostly experimental research was conducted on the topic of cavitation erosion [8, 9]. With the emergence of computational fluid dynamics (CFD) the focus shifted to formulating numerical models to be used in conjunction with CFD for prediction of cavitation erosion in hydraulic systems. Fortes-Patella et al. [10] and Pereira [11] formulated an energy cascade model to describe the transfer of potential energy of cavitation to the solid surface based on the previous experimental work by Hammitt [8] and Vogel et al. [9].

A completely different approach to cavitation erosion modelling, based on the microjet hypothesis, has been proposed by Dular and Coutier-Delgosha [12]. Based on that modelling approach, Peters and Moctar [13] presented a new cavitation erosion model coupled with a multiscale approach to cavitation modelling. A modified version of this cavitation erosion model was presented by Mohammadkhani and Alizadeh [14] and applied for the axisymmetric nozzle.

Another approach to study the cavitation erosion was presented in the paper by Biluš et al. [15], where four cavitation collapse structures present in the cavitating flow through a Venturi

channel were analysed. A fully compressible flow was considered in order to accurately predict pressure peaks on the surface of the channel.

The main advantage of the proposed energy cascade model is that it obeys the physical energy transfer phenomena [16]. This is recognised in the literature, as different versions and implementations have now been successfully used to predict cavitation erosion in various cases. Usta and Korkut [17] presented cavitation erosion prediction with a version of the cavitation erosion model termed Erosive Power Method (EPM) on NACA 0015 hydrofoil and marine propeller and concluded that there was good agreement between prediction from CFD simulation and experiment. Their work later focused on marine propellers [3]. Comparison of different versions of cavitation erosion model (different erosion indicators) to predict cavitation erosion on a hydrofoil was conducted by Geng et al. [18]. Similarly Mo et al. [19] compared different erosion indicators to predict cavitation erosion in high-speed gears.

However, some uncertainty emerged regarding the numerical implementation of the cavitation energy cascade model, namely the calculation of the energy received by a given surface element, the numerical error in the calculation of cavitation potential energy and the definition of the cavitation collapse driving pressure.

Leclercq et al. [20] used the solid angle to account for the transfer of cavitation potential energy to the surface by way of a pressure wave. Whereas Leclercq et al. [20] used the analytical expression for the solid angle which was derived in [21] to project the radiated power on a triangular surface element, Schenke and van Terwisga [22] used a fully continuous form of the solid angle projection, which represents the surface specific impact power at a point location. Melissaris et al. [23] and Pezdevsek et al. [24] observed that when the source is extremely close to the surface the discrete approximation of the solid angle can lead to solid angles orders of magnitude larger than the maximum solid angle.

Melissaris et al. [25] also derived three formulations for the calculation of cavitation potential energy and compared their accuracy in the case of a marine propeller. The formulation with the mass transfer source term and the formulation with the partial derivative of vapour volume fraction produced comparable results and agreed well with the experiment, while the formulation with the velocity divergence showed significant deviation from the other two formulations and the experiment. Kevorkijan et al. [26] compared the three formulations in the case of cavitation in an axisymmetric nozzle and also found that the results obtained by the velocity divergence formulation deviated significantly from the other two formulations and the experiment.

With regards to the cavitation collapse driving pressure, Leclercq et al. [20] used the instantaneous cell pressure as this reflects the local conditions. On the other hand, Schenke and van Terwisga [22, 27] used the time average of the local pressure to avoid the influence of cavitation dynamics. Arabnejad et al. [28] instead used a different method that is based on the kinetic energy in the surrounding liquid during the collapse rather than the potential energy of collapsing cavities, which avoids the uncertainty regarding the calculation of the collapse driving pressure.

In the present work a cavitation erosion model has been applied to a benchmark hydrofoil NACA 0018-45 and different definitions of driving pressure. Calculations of cavitation potential energy are compared with the goal to understand the influence of driving pressure definition on cavitation erosion prediction, since understanding the influence of driving pressure definition is crucial for better cavitation erosion prediction.

2. GOVERNING EQUATIONS

Homogenous mixture flow in Ansys CFX is described by the following set of equations. Phases are considered incompressible and share the same velocity field $\vec{u}$.

The continuity equation can be written as:

$$\nabla \cdot \vec{u} = \dot{m}\left(\frac{1}{\rho_\mathrm{l}} + \frac{1}{\rho_\mathrm{v}}\right) \tag{1}$$

where $\vec{u}$ is the time averaged mixture velocity, $\dot{m}$ is the interphase mass transfer rate due to cavitation, ρ_v is the vapour density and ρ_l is the liquid density.

For the liquid vapour mixture the momentum equation is written as:

$$\frac{\partial(\rho\vec{u})}{\partial t} + \nabla \cdot (\rho\vec{u}\vec{u}) = -\nabla p + \nabla \cdot \left((\mu + \mu_\mathrm{t})(\nabla\vec{u} + (\nabla\vec{u})^T)\right) \tag{2}$$

where ρ is the density of the water-vapour mixture, p is the time averaged pressure, μ is the dynamic viscosity of the water-vapour mixture and μ_t is the turbulent viscosity.

Volume fraction equation for the vapour phase is defined as:

$$\frac{\partial\alpha}{\partial t} + \nabla \cdot (\alpha\vec{u}) = \frac{\dot{m}}{\rho_\mathrm{v}} \tag{3}$$

where α is the vapour volume fraction.

2.1 Turbulence model

Menter [29] proposed the use of the SST turbulence model which is a combination of the *k-ε* model for the outer region and *k-ω* model for the area near the surface. The model implements a transformation from the *k-ε* model to a *k-ω* formulation. This is performed using a blending function F_1, where F_1 is equal to one near the surface and it decreases to zero outside the boundary layer. The turbulent viscosity is altered to consider for the transport of the turbulent shear stress. The turbulent viscosity is defined as:

$$\mu_t = \frac{\rho\, a_1 k}{\max(a_1\omega, SF_2)} \tag{4}$$

where k is the turbulent kinetic energy, ω is the specific dissipation rate, S is the strain rate magnitude, a_1 is the constant (0.31 [29]) and F_2 is the second blending function.

Two-equation turbulence models were developed for single phase flows and they tend to overpredict the turbulent viscosity in the region where both the vapour and liquid phase are present, which causes the damping of cavitation dynamics [16, 30].

Reboud et al. [31, 32] proposed a modification of the *k-ε* turbulence model by reducing the turbulent viscosity to consider the suggested two-phase flow effects on the turbulent structures [16, 30]. The density in the turbulent viscosity equation is now replaced with a density function and is written as:

$$f(\rho) = \rho_\mathrm{v} + \frac{(\rho - \rho_\mathrm{v})^n}{(\rho_\mathrm{l} - \rho_\mathrm{v})^{n-1}} \tag{5}$$

where ρ is the mixture density and n is a constant (10 [16, 32]).

2.2 Cavitation model

Schnerr and Sauer [33] proposed that the vapour formation consists of spherical bubbles. The spherical bubbles are governed by the simplified Rayleigh Plesset equation. The mass transfer rate is proportional to $\alpha(1-\alpha)$:

$$\dot{m} = \begin{cases} F_\mathrm{vap}\dfrac{\rho_\mathrm{v}\rho_\mathrm{l}}{\rho}\alpha(1-\alpha)\dfrac{3}{R_\mathrm{B}}\sqrt{\dfrac{2}{3}\dfrac{p_\mathrm{v}-p}{\rho_\mathrm{l}}} & \text{if } p < p_\mathrm{v} \\ F_\mathrm{cond}\dfrac{\rho_\mathrm{v}\rho_\mathrm{l}}{\rho}\alpha(1-\alpha)\dfrac{3}{R_\mathrm{B}}\sqrt{\dfrac{2}{3}\dfrac{p-p_\mathrm{v}}{\rho_\mathrm{l}}} & \text{if } p > p_\mathrm{v} \end{cases} \tag{6}$$

where p_v is the vapour saturation pressure, R_B is the bubble radius, F_vap is the evaporation coefficient and F_cond is the condensation coefficient.

The bubble radius is defined as:

$$R_\mathrm{B} = \left(\frac{\alpha}{1-\alpha}\frac{3}{4\pi n_\mathrm{B}}\right)^{\frac{1}{3}} \tag{7}$$

where n_B is the bubble number density. The proposed values [33] for the two coefficients are $F_\mathrm{vap} = 1$ and $F_\mathrm{cond} = 0.2$. The proposed value [16] for the bubble number density is $n_\mathrm{B} = 10^{13}$.

2.3 Cavitation erosion potential

We can calculate the potential energy of vapour structures E_pot as based on the work of [10, 11]:

$$E_\mathrm{pot} = (p - p_\mathrm{v})V_\mathrm{v} \tag{8}$$

where V_v is the volume of the vapour structure.

The potential power of vapour structures P_pot can be separated in two terms, the first term considers the contribution of the void fraction derivative and the second term that takes into account the pressure derivative:

$$P_\mathrm{pot} = -\frac{dE_\mathrm{pot}}{dt} = P_\mathrm{pot}|_{p=\mathrm{const.}} + P_\mathrm{pot}|_{\alpha=\mathrm{const.}} \tag{9}$$

For the void fraction derivative term the potential power is defined as:

$$P_\mathrm{pot}|_{p=\mathrm{const.}} = -(p - p_\mathrm{v})\left(\frac{dV_\mathrm{v}}{dt}\right) \tag{10}$$

Inside the volume of an element V_cell the vapour fraction is defined as:

$$\alpha = \frac{V_\mathrm{v}}{V_\mathrm{cell}} = \frac{\rho}{\rho_\mathrm{l} - \rho_\mathrm{v}} \tag{11}$$

The void fraction derivative term for the potential power can be rewritten as:

$$P_\mathrm{pot}|_{p=\mathrm{const.}} = -(p - p_\mathrm{v})V_\mathrm{cell}\left(\frac{d\alpha}{dt}\right) \tag{12}$$

For the pressure derivative term the potential power is defined as:

$$P_\mathrm{pot}|_{\alpha=\mathrm{const.}} = -V_\mathrm{v}\left(\frac{dp_\mathrm{d}}{dt}\right) \tag{13}$$

The potential power of vapour structures can be rewritten as:

$$P_\mathrm{pot} = -(p - p_\mathrm{v})V_\mathrm{cell}\left(\frac{d\alpha}{dt}\right) - V_\mathrm{v}\left(\frac{dp_\mathrm{d}}{dt}\right) \tag{14}$$

The negative sign is needed to ensure a positive value for the instantaneous potential power. A reduction in cavitation erosion potential represents a vapour cavity collapse. We considered only the collapse stage in the model and assume that the vapour structure is aggressive if $P_\mathrm{pot} > 0$. We calculated both terms and came to the same conclusion as other authors [20, 34] that the void derivative term is dominant $\left\|P_\mathrm{pot}|_{\alpha=\mathrm{const.}}\right\| \ll \left\|P_\mathrm{pot}|_{p=\mathrm{const.}}\right\|$ and so the pressure derivative term can be ignored.

In the study we used three equation formulations for the potential power, a formulation reliant on the vapour volume fraction $P_{\mathrm{pot},\alpha}$, a formulation reliant on the velocity divergence $P_\mathrm{pot,div}$ and a formulation reliant on the vapour phase source term $P_\mathrm{pot,source}$.

2.4 Derivative

The potential power of vapour structures dependent on the vapour volume fraction can be defined as:

$$P_{\mathrm{pot},\alpha} = -(p - p_{\mathrm{v}})V_{\mathrm{cell}}\left(\frac{d\alpha}{dt}\right) \tag{15}$$

2.5 Divergence

If we take into account the Lagrangian time derivative:

$$\frac{d\rho}{dt} + \rho\ \mathrm{div}(\boldsymbol{U}) = 0 \tag{16}$$

we can define the potential power of vapour structures dependent on the velocity divergence as:

$$P_{\mathrm{pot,div}} = -(p - p_{\mathrm{v}})V_{\mathrm{cell}}\frac{\rho}{\rho_{\mathrm{l}} - \rho_{\mathrm{v}}}\ \mathrm{div}(\boldsymbol{U}) \tag{17}$$

2.6 Source term

We can define the potential power of vapour structures dependent on the source term as:

$$P_{\mathrm{pot,source}} = -(p - p_{\mathrm{v}})V_{\mathrm{cell}}\frac{\rho}{\rho_{\mathrm{l}}}\ S_{\alpha} \tag{18}$$

The source term is defined as:

$$S_{\alpha} = \frac{\dot{m}}{\rho_{\mathrm{v}}} \tag{19}$$

2.7 Driving pressure

In cavitation the driving pressure is the pressure that is driving the collapse of the vapour structure. In general, the driving pressure defines the amount of energy released during last phase of cavitation. How to correctly define the driving pressure from a modelling perspective, can be a subject of debate [20, 22, 27, 28]. In this study we used different approaches to determine the driving pressure.

The first approach defines the driving pressure as the reference pressure, this takes the least computational resources since it is a constant value for all cells and is defined at the start of the simulation. In this approach the pressure is constant across the entire domain which may lead to inaccurate results.

The second approach defines the driving pressure as the pressure inside the cell at the calculated time step.

The third approach defines the driving pressure in a cell as an average pressure value in that cell across one shedding cycle. This takes the most computational resources since we need to load all the time steps of the shedding cycle and then average the pressure values for each cell.

The fourth approach defines the driving pressure as the pressure values for each cell taken directly from steady state simulations. Since steady state values are in some way time averaged values, we think we might get similar result to the approach described above where we averaged pressure values in a cell across one shedding cycle. This approach requires less computational resources since we don't need to load the results for all time steps but only the steady state values.

2.8 Potential power applied to the surface

Based on the work in [20] and [35] the potential power applied to each surface element j and for all volume elements i is defined as:

$$P_{\mathrm{mat_j}} = \frac{1}{\Delta S_\mathrm{j}} \sum_{i|\overrightarrow{Xs_\mathrm{j}Xcell_\mathrm{i}}\cdot\overrightarrow{n_\mathrm{j}}>0} \frac{\Omega_\mathrm{ij}}{4\pi} P_{\mathrm{pot_i}} \tag{20}$$

where ΔS_j is the area of a surface element, $\overrightarrow{Xs_\mathrm{j}Xcell_\mathrm{i}}$ is the vector from the centre of the surface element j to the centre of the volume element i and $\overrightarrow{n_\mathrm{j}}$ is the normal vector of the surface element j. The solid angle Ω is defined as the area that an element projects on a sphere divided by the radius of the sphere. It is essentially a measure of the amount of the field of view and in our case, it will quantify the distance and angle from an energy source to the surface element:

$$\Omega = \frac{A}{r^2} \tag{21}$$

where A is the area on the sphere and r is the sphere radius.

For the solid angle of a planar triangle an analytical expression was derived by Van Oosterom and Strackee [21] and is written as:

$$\tan\left(\frac{1}{2}\Omega\right) = \frac{\overrightarrow{R_1}\cdot\left(\overrightarrow{R_2}\times\overrightarrow{R_3}\right)}{R_1R_2R_3 + \left(\overrightarrow{R_1}\cdot\overrightarrow{R_2}\right)R_3 + \left(\overrightarrow{R_1}\cdot\overrightarrow{R_3}\right)R_2 + \left(\overrightarrow{R_2}\cdot\overrightarrow{R_3}\right)R_1} \tag{22}$$

For all the time steps we can add up the potential power applied to each surface and then divide by the number of time steps to get the mean loading $P_{\mathrm{mean,mat}}$ which represents a qualitative representation of the eroded region:

$$\frac{P_{\mathrm{mean,mat}}}{\Delta S_\mathrm{j}} = \frac{1}{N}\sum_{i=1}^{N}\frac{P_{\mathrm{mat_j}}}{\Delta S_\mathrm{j}} \tag{23}$$

3. NUMERICAL TEST CASE AND SETUP

3.1 Geometry

The hydrodynamic profile NACA 0018-45 was chosen for this study, it is a modified four-digit NACA 0018 profile which is indicated by the 45 digits. The chord length for the profile was defined at 60 mm and an angle of attack of 6.5°. The computational domain size was set at 2 chord lengths before the leading edge, 5 chord lengths after the leading edge and the height of the domain was 1.33 chord lengths. The width of the domain was set at 40 mm.

3.2 Mesh

A block-structured mesh which was created in ICEM CFD is presented in Fig. 1. The geometry of the hydrodynamic profile was defined with 214 elements while the whole profile surface had 7200 elements. The final mesh had approximately 765.000 elements. For the elements near the profile surface the condition y+<1 was prioritised.

3.3 Boundary conditions

The left surface was defined as an inlet with a normal velocity of 24.2 m/s. The right surface was defined as an outlet with a static pressure of 213.115 kPa. The bottom, top, side surfaces and the surface of the hydrodynamic profile were defined as no slip walls.

Transient simulations were conducted in Ansys CFX. The time step for the simulation was defined 10^{-5} second. The convergence criterion for the RMS residuals was defined as 10^{-6}. We defined the maximum number of iterations within a time step at 50. The SST turbulence model was used with the Reboud's correction. For the Schnerr-Sauer cavitation model the default values for the coefficients were used. The vapour saturation pressure (p_v) was set at 2811 Pa.

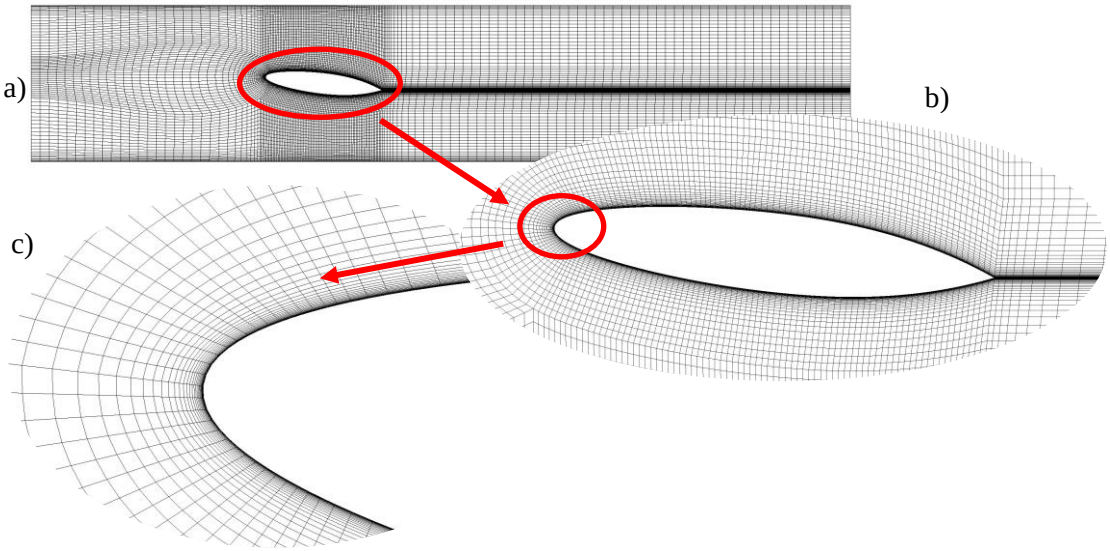

Figure 1: a) surface mesh of the whole domain, b) a cropped area of the mesh, c) a close up of the leading edge.

Results from Ansys CFX 2020 R2 were imported into Matlab 2022b where we calculated the mean potential power applied to each surface element for all potential power formulations and all driving pressure approaches.

4. RESULTS

The total vapour volume in the computational domain is shown in Fig. 2 for the time interval 0 ms to 83 ms. From the figure we can see that the total vapour volume in the domain changes periodically, which confirms the transient nature of the extent of cavitation. Within the simulated time multiple vapour structure shedding events occurred. To reduce the computational time for this study, we only focused on one shedding cycle from 47.25 ms to 65.25 ms as seen in Fig. 2.

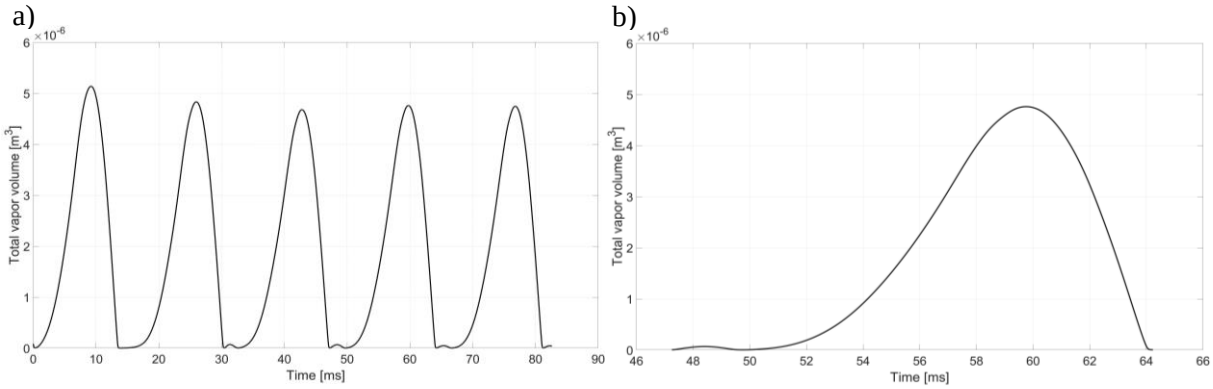

Figure 2: a) Total vapour volume in the domain, b) total vapour volume in the domain for the selected shedding cycle.

In Fig. 3 we see the mean potential power distribution on the hydrofoil surface for the derivative formulation. The maximum mean potential power values were located at the trailing edge which corresponds well with experimental data from literature [16]. The distribution of the mean potential power on the hydrofoil surface does not differ significantly for all the driving pressure approaches used. The difference is in the absolute values which are notably lower in the second approach where the driving pressure is the pressure inside the cell at the calculated time step. For all other approaches the values are similar which in the case of the reference

pressure approach is surprising since we expected it to differ more significantly from pressure averaged result.

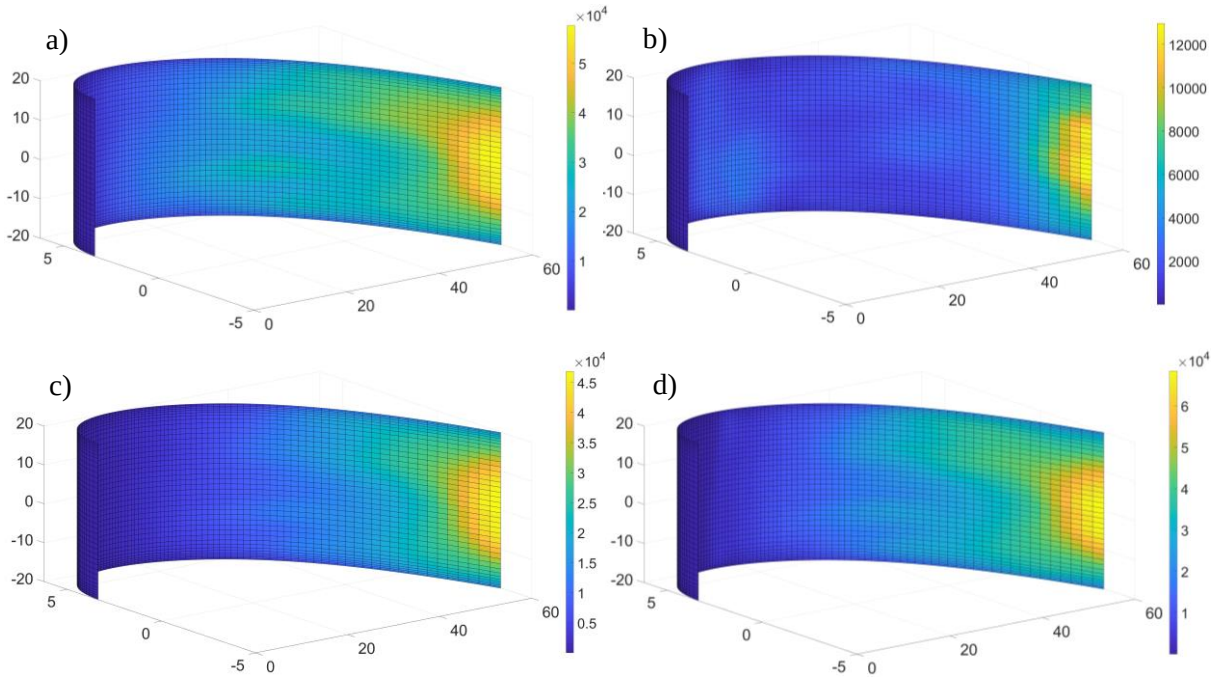

Figure 3: Derivative formulation for a) reference pressure, b) no pressure average, c) pressure average across all time steps and d) steady state.

In Fig. 4 we see the mean potential power distribution on the hydrofoil surface for the divergence formulation. The maximum mean potential power values were located at the trailing edge which corresponds well with experimental data from literature [16]. The distribution of the mean potential power on the hydrofoil surface does not differ significantly for all the driving pressure approaches used. The difference in the absolute values do not differ significantly.

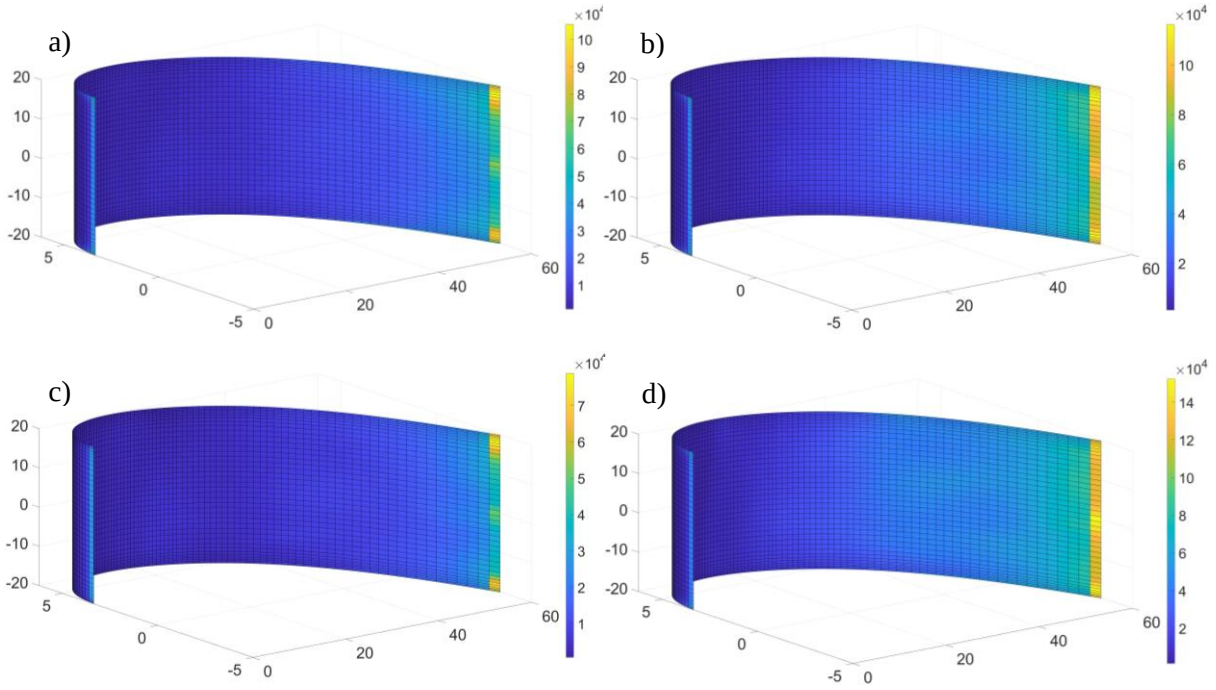

Figure 4: Divergence formulation for a) reference pressure, b) no pressure average, c) pressure average across all time steps and d) steady state.

In Fig. 5 we see the mean potential power distribution on the hydrofoil surface for the source formulation. For all driving pressure approaches except for the reference pressure approach the maximum mean potential power values were located at the trailing edge which corresponds well with experimental data from literature [16]. For the reference pressure approach the maximum mean potential power values are near the leading-edge witch not only differs from other approaches but also from experimental data [16]. The difference for the other approaches is in the absolute values which are notably lower in the second approach where the driving pressure is the pressure inside the cell at the calculated time step for this case the distribution of the mean potential power applied to the surface also differs. For the steady state and pressure averaged results the values and the mean potential power distribution on the hydrofoil surface are fairly similar.

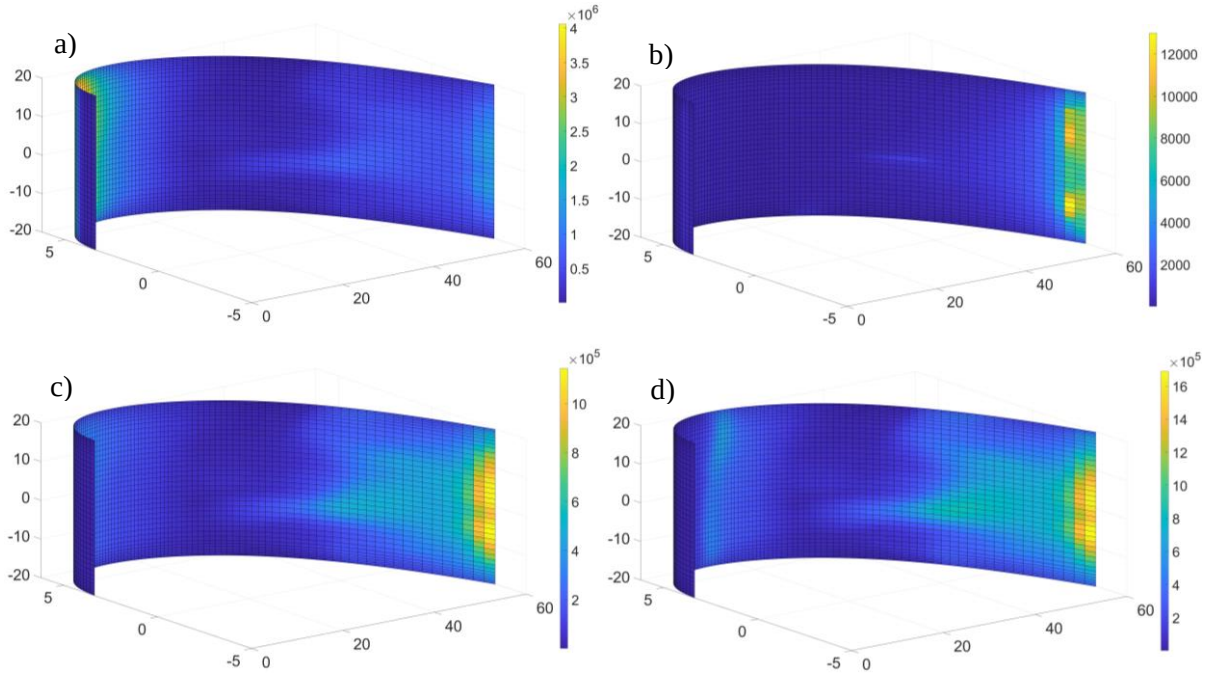

Figure 5: Source formulation for a) reference pressure, b) no pressure average, c) pressure average across all time steps and d) steady state.

5. CONCLUSION

Transient simulations were performed in Ansys CFX with a time step of 1e-5 s. From the simulation data we saw that the total vapour volume in the domain changes periodically, which confirms the transient nature of the extent of cavitation. Within the simulated time of 80 ms multiple vapour cloud shedding events occurred. An FFT analysis was done on the total vapour volume data and the shedding frequency was calculated at 59 Hz, which is similar to results from literature [16].

An appropriate description of cavitation dynamics is crucial. The Schnerr-Sauer cavitation model predicts the extent and dynamics of cavitation correctly. Based on the results the vapour structure collapses happened at or near the trailing edge so we can expect the cavitation erosion to be the highest at that location.

Result from the transient simulation in Ansys CFX were imported into Matlab where the mean potential power distribution on the hydrofoil surface was calculated for the derivative, divergence and source term form. For all three potential power forms the driving pressure was defined by four different approaches. The first approach defines the driving pressure as the reference pressure, the second approach defines the driving pressure as the pressure inside the

cell at the calculated time step, the third approach defines the driving pressure in a cell as an average pressure value in that cell across one shedding cycle and the last approach defines the driving pressure as the pressure values for each cell taken directly from steady state simulations.

The results of the study show that for all terms the averaged pressure values from all timesteps in one shedding cycle and steady state pressure values give similar results in terms the mean potential power distribution on the hydrofoil surface and in absolute values of the mean potential power. The reference pressure approach gave similar result for the derivative and divergence formulation while for the source term the maximum mean potential power values were located near the leading edge, which is in contradiction to experimental data and other approaches. The approach where we used no pressure averaging gives adequate results in terms of the mean potential power distribution on the hydrofoil surface but differs from other approaches in absolute values which are considerably lower for all terms.

For this study we can conclude that the averaged pressure values from all timesteps in one shedding cycle and steady state pressure values provide consistent results independent of the potential power form and can thus be recommended. If we consider the computational resources needed for both approaches, we recommend using the steady state approach. For a more concrete result, specifically in the case of the reference pressure approach to define the driving pressure in combination with the source term formulation of cavitation potential power, further analysis on different cases with different cavitating flow regimes is needed.

REFERENCES

[1] Zhou, R.; Chen, H.; Dong, L.; Liu, H.; Chen, Z.; Zhang, Y.; Cheng, Z. (2022). Effect of vibration and noise measuring points distribution on the sensitivity of pump cavitation diagnosis, *Strojniski vestnik – Journal of Mechanical Engineering*, Vol. 68, No. 5, 325-338, doi:10.5545/sv-jme.2022.59

[2] Lešnik, L.; Kegl, B.; Torres-Jiménez, E.; Cruz-Peragón, F.; Mata, C.; Biluš, I. (2021). Effect of the in-cylinder back pressure on the injection process and fuel flow characteristics in a common-rail diesel injector using GTL fuel, *Energies*, Vol. 14, No. 2, Paper 452, 21 pages, doi:10.3390/en14020452

[3] Köksal, Ç. S.; Usta, O.; Aktas, B.; Atlar, M.; Korkut, E. (2021). Numerical prediction of cavitation erosion to investigate the effect of wake on marine propellers, *Ocean Engineering*, Vol. 239, Paper 109820, 19 pages, doi:10.1016/j.oceaneng.2021.109820

[4] Melissaris, T.; Schenke, S.; van Terwisga, T. J. C. (2023). Cavitation erosion risk assessment for a marine propeller behind a Ro-Ro container vessel, *Physics of Fluids*, Vol. 35, No. 1, Paper 013342, 22 pages, doi:10.1063/5.0131914

[5] Morgut, M.; Jošt, D.; Škerlavaj, A.; Nobile, E.; Contento, G. (2018). Numerical predictions of cavitating flow around a marine propeller and Kaplan turbine runner with calibrated cavitation models, *Strojniski vestnik – Journal of Mechanical Engineering*, Vol. 64, No. 9, 543-554, doi:10.5545/sv-jme.2017.4647

[6] Lord Rayleigh (1917). VIII. On the pressure developed in a liquid during the collapse of a spherical cavity, *The London, Edinburgh, and Dublin Philosophical Magazine and Journal of Science*, Series 6, Vol. 34, No. 200, 94-98, doi:10.1080/14786440808635681

[7] Plesset, M. S. (1949). The dynamics of cavitation bubbles, *Journal of Applied Mechanics*, Vol. 16, No. 3, 277-282, doi:10.1115/1.4009975

[8] Hammitt, F. G. (1962). *Observations on Cavitation Damage in a Flowing System*, Internal Report No. 14, National Aeronautics and Space Administration, Washington D. C.

[9] Vogel, A.; Lauterborn, W.; Timm, R. (1989). Optical and acoustic investigations of the dynamics of laser-produced cavitation bubbles near a solid boundary, *Journal of Fluid Mechanics*, Vol. 206, 299-338, doi:10.1017/S0022112089002314

[10] Fortes-Patella, R.; Reboud, J. L.; Briancon-Marjollet, L. (2004). A phenomenological and numerical model for scaling the flow aggressiveness in cavitation erosion, *Cavitation Erosion Workshop*, Paper 2968, 36 slides

[11] Pereira, F. (1997). *Prediction de l'erosion de cavitation: approche energetique*, PhD Thesis, Ecole Polytechnique Federale de Lausanne, Lausanne
[12] Dular, M.; Coutier-Delgosha, O. (2009). Numerical modelling of cavitation erosion, *International Journal for Numerical Methods in Fluids*, Vol. 61, No. 12, 1388-1410, doi:10.1002/fld.2003
[13] Peters, A.; el Moctar, O. (2020). Numerical assessment of cavitation-induced erosion using a multi-scale Euler–Lagrange method, *Journal of Fluid Mechanics*, Vol. 894, Paper A19, 54 pages, doi:10.1017/jfm.2020.273
[14] Mohammadkhani, A.; Alizadeh, M. (2021). Numerical prediction of hydrodynamic cavitating flow structures and their corresponding erosion, *Journal of Hydrodynamics*, Vol. 33, No. 3, 546-571, doi:10.1007/s42241-021-0056-2
[15] Biluš, I.; Hočevar, M.; Dular, M.; Lešnik, L. (2020). Numerical prediction of various cavitation erosion mechanisms, *Journal of Fluids Engineering*, Vol. 142, No. 4, Paper 041402, 8 pages, doi:10.1115/1.4045365
[16] Li, Z. (2012). *Assessment of Cavitation Erosion with a Multiphase Reynolds-Averaged Navier-Stokes Method*, PhD Thesis, TU Delft, Delft
[17] Usta, O.; Korkut, E. (2019). Prediction of cavitation development and cavitation erosion on hydrofoils and propellers by Detached Eddy Simulation, *Ocean Engineering*, Vol. 191, Paper 106512, 19 pages, doi:10.1016/j.oceaneng.2019.106512
[18] Geng, L.; Zhang, D.; Chen, J.; De La Torre, O.; Escaler, X. (2022). Prediction of cavitation erosion with different erosion risk indicators, *Ocean Engineering*, Vol. 247, Paper 110633, 13 pages, doi:10.1016/j.oceaneng.2022.110633
[19] Mo, X.; Wang, J.; Cheng, L.; Ouyang, T. (2023). Numerical prediction of vibration-induced cavitation erosion in high-speed gears using erosion risk indicators, *Tribology International*, Vol. 179, Paper 108122, 22 pages, doi:10.1016/j.triboint.2022.108122
[20] Leclercq, C.; Archer, A.; Fortes-Patella, R.; Cerru, F. (2017). Numerical cavitation intensity on a hydrofoil for 3D homogeneous unsteady viscous flows, *International Journal of Fluid Machinery and Systems*, Vol. 10, No. 3, 254-263, doi:10.5293/ijfms.2017.10.3.254
[21] Van Oosterom, A.; Strackee, J. (1983). The solid angle of a plane triangle, *IEEE Transactions on Biomedical Engineering*, Vol. BME-30, No. 2, 125-126, doi:10.1109/tbme.1983.325207
[22] Schenke, S.; van Terwisga, T. J. C. (2019). An energy conservative method to predict the erosive aggressiveness of collapsing cavitating structures and cavitating flows from numerical simulations, *International Journal of Multiphase Flow*, Vol. 111, 200-218, doi:10.1016/j.ijmultiphaseflow.2018.11.016
[23] Melissaris, T.; Schenke, S.; Bulten, N.; van Terwisga, T. J. C. (2022). Cavitation erosion risk assessment on a full-scale steerable thruster, *Ocean Engineering*, Vol. 251, Paper 111019, 16 pages, doi:10.1016/j.oceaneng.2022.111019
[24] Pezdevsek, M.; Kevorkijan, L.; Bilus, I. (2022). Cavitation erosion modelling – comparison of two solid angle projection approaches, *International Journal of Simulation Modelling*, Vol. 21, No. 2, 249-260, doi:10.2507/IJSIMM21-2-600
[25] Melissaris, T.; Schenke, S.; Bulten, N.; van Terwisga, T. J. C. (2020). On the accuracy of predicting cavitation impact loads on marine propellers, *Wear*, Vols. 456-457, Paper 203393, 18 pages, doi:10.1016/j.wear.2020.203393
[26] Kevorkijan, L.; Lešnik, L.; Biluš, I. (2022). Cavitation erosion modelling on a radial divergent test section using RANS, *Strojniski vestnik – Journal of Mechanical Engineering*, Vol. 68, No. 2, 71-81, doi:10.5545/sv-jme.2021.7364
[27] Melissaris, T.; Bulten, N.; van Terwisga, T. (2018). On cavitation aggressiveness and cavitation erosion on marine propellers using a URANS method, *Proceedings of the 10th International Symposium on Cavitation (CAV2018)*, 838-843, doi:10.1115/1.861851_ch160
[28] Arabnejad, M. H.; Svennberg, U.; Bensow, R. E. (2021). Numerical assessment of cavitation erosion risk using incompressible simulation of cavitating flows, *Wear*, Vols. 464-465, Paper 203529, 16 pages, doi:10.1016/j.wear.2020.203529
[29] Menter, F. R. (1994). Two-equation eddy-viscosity turbulence models for engineering applications, *AIAA Journal*, Vol. 32, No. 8, 1598-1605, doi:10.2514/3.12149

[30] Sorgüven, E.; Schnerr, G. H. (2003). Modified *k-ω* model for simulation of cavitating flows, *Proceedings in Applied Mathematics and Mechanics*, Vol. 2, No. 1, 386-387, doi:10.1002/pamm.200310177
[31] Reboud, J. L.; Stutz, B.; Coutier-Delgosha, O. (1998). Two-phase flow structure of cavitation: experiment and modeling of unsteady effects, *Third International Symposium on Cavitation*, 7 pages
[32] Coutier-Delgosha, O.; Fortes-Patella, R.; Reboud, J. L. (2002). Simulation of unsteady cavitation with a two-equation turbulence model including compressibility effects, *Journal of Turbulence*, Vol. 3, Paper N58, 20 pages, doi:10.1088/1468-5248/3/1/058
[33] Schnerr, G. H.; Sauer, J. (2001). Physical and numerical modeling of unsteady cavitation dynamics, *4th International Conference on Multiphase Flow*, 12 pages
[34] Fortes Patella, R.; Archer, A.; Flageul, C. (2012). Numerical and experimental investigations on cavitation erosion, *IOP Conference Series: Earth and Environmental Science*, Vol. 15, No. 2, Paper 022013, 12 pages, doi:10.1088/1755-1315/15/2/022013
[35] Krumenacker, L.; Fortes-Patella, R.; Archer, A. (2014). Numerical estimation of cavitation intensity, *IOP Conference Series: Earth and Environmental Science*, Vol. 22, No. 5, Paper 052014, 11 pages, doi:10.1088/1755-1315/22/5/052014